Petroleum Science 22 (2025) 4975–4991

Contents lists available at ScienceDirect

Petroleum Science

journal homepage: www.keaipublishing.com/en/journals/petroleum-science

Original Paper

Inversion methods for elastic parameters and fracture parameters of monoclinic media induced by two groups of inclined fractures

Sheng-Zhao Dai [a, b], Guang-Zhi Zhang [a, b, *], Hong-Jian Hao [a, b], Zhen-Yu Zhu [c], Zhen-Feng Liu [d], Zhen Yang [d]

[a] Key Laboratory of Deep Oil and Gas, China University of Petroleum (East China), Qingdao, 266580, Shandong, China
[b] School of Geoscience, China University of Petroleum (East China), Qingdao, 266580, Shandong, China
[c] CNOOC Research Institute Co., Ltd., Beijing, 100028, China
[d] Sinopec Petroleum Exploration and Production Research Institute, Beijing, 100083, China

ARTICLE INFO

Article history:
Received 14 November 2024
Received in revised form
23 January 2025
Accepted 9 May 2025
Available online 10 May 2025

Edited by Meng-Jiao Zhou

Keywords:
Fracture
Monoclinic anisotropic medium
Reflection coefficient equation
Inversion

ABSTRACT

Fractures significantly impact oil and gas production by altering the mechanical properties of subsurface rocks. This study investigates the forward and inverse problems associated with monoclinic anisotropic media, which arise from the presence of two sets of inclined fractures within an isotropic matrix. We first derive the stiffness matrix for this monoclinic medium by applying Schoenberg's linear slip theory. Subsequently, we employ the point spread function and the steady phase method to derive and simplify the reflection coefficient equation for seismic waves interacting with this complex medium. Finally, we verify the rationality of the method by using synthetic seismic records and actual seismic records. The proposed equations and inversion techniques offer a more accurate framework for characterizing monoclinic anisotropic media affected by inclined fractures, thereby enhancing the interpretation of subsurface structures in hydrocarbon exploration.

1. Introduction

Fractures are crucial pathways for oil and gas migration in tight reservoirs, fundamentally influencing the mechanical properties of the subsurface medium (Guo et al., 2022a; Pan and Zhao, 2024). The presence of fractures introduces anisotropy, meaning that the velocity of seismic waves varies with direction. For a medium that includes only one set of fractures, it can often be modeled as having horizontal transverse isotropy (HTI) (Rüger, 1997; Bakulin et al., 2000a; Chen et al., 2017; Li et al., 2024), vertical transverse isotropy (VTI) (Rüger, 1998; Jílek, 2002; Shaw and Sen, 2004; Guo et al., 2022b), or tilted transverse isotropy (TTI) (Pan et al., 2021; Zhao et al., 2024), depending on the orientation of the fractures. When a medium contains multiple sets of fractures, the symmetry decreases, leading to more complex anisotropic media such as orthotropic (Pan et al., 2019; Zhang et al., 2020), monoclinic anisotropic (Bakulin et al., 2000b; Pan et al., 2022), and even highly anisotropic media. In such complex cases, the number of independent elastic parameters increases, making the inversion process more challenging. In this paper, we address the forward and inversion problems associated with monoclinic anisotropic media, specifically those characterized by two sets of incoherent inclined fractures. By exploring the implications of these complexities, we aim to advance the understanding and characterization of subsurface structures, which is essential for optimizing oil and gas exploration and production.

Understanding fracture density and fracture inclination angle is crucial for evaluating the degree of fracture development and optimizing the placement of oil and gas wells. The influence of fractures on the medium has been extensively studied, with seminal contributions including Schoenberg's linear slip theory (Schoenberg, 1980). To quantitatively assess the anisotropic behavior of fractures, Schoenberg and Sayers posit that fractures exhibit rotational invariance, building on this premise, they introduce the concepts of normal and tangential weakness to elucidate the influence of fractures on material properties (Schoenberg and

* Corresponding author.
E-mail address: zhanggz@upc.edu.cn (G.-Z. Zhang).
Peer review under the responsibility of China University of Petroleum (Beijing).

https://doi.org/10.1016/j.petsci.2025.05.005
1995-8226/

Sayers, 1995). This theoretical framework provides a robust basis for understanding the complex interactions between fractures and the mechanical behavior of geological formations. Building on this foundational work, Bakulin et al. (2000a) further developed the theory by exploring the relationships between normal and tangential weaknesses, Thomsen's anisotropy parameters, and fracture density.

Elastic impedance inversion has become a widely used technique in geophysical exploration due to its effectiveness. According to Cambois, the process involves two main steps: first, inverting the angular elastic impedance Based on logging data, and then extracting elastic parameters from the resulting impedance data (Cambois, 2000). Zong et al. successfully applied this method to extract Young's modulus and Poisson's ratio, yielding promising results (Zong et al., 2013). In anisotropic media, Martins first derived the elastic impedance equation for weakly anisotropic materials (Martins, 2006), while Chen et al. (2014) derived the elastic impedance equation for HTI media induced by vertical fractures and orthogonal anisotropic media with vertical fractures developed in shale background, and based on the equation, Chen et al. (2017) studied the azimuthal elastic impedance inversion research, leading to improved reservoir prediction accuracy.

In this study, we derive the reflection coefficient equation for a monoclinic medium that results from embedding two sets of inclined fractures within an isotropic medium. This derivation is based on weak anisotropy approximation and equivalent medium theory, combined with scattering theory and the steady-state phase method. To address the challenge posed by numerous inversion parameters, we simplify the reflectance coefficient equation using Bakulin's research insights (Bakulin et al., 2000a). Subsequently, we establish an azimuthal elastic impedance inversion equation and validate its effectiveness using well data and real-world datasets.

2. Theory and method

2.1. Derivation of the reflection coefficient equation

Similar to VTI media, the stiffness matrix of TTI media, which incorporates a set of tilted fractures embedded within isotropic materials, can be expressed as follows:

$$\mathbf{C}^{\mathrm{TTI}} = \mathbf{C}^{\mathrm{Iso}} + \mathbf{C}^{\mathrm{T}} \tag{1}$$

where $\mathbf{C}^{\mathrm{Iso}}$ represents the stiffness matrix of the background isotropic materials as:

$$\mathbf{C}^{\mathrm{Iso}} = \begin{bmatrix} M_b & \lambda_b & \lambda_b & 0 & 0 & 0 \\ \lambda_b & M_b & \lambda_b & 0 & 0 & 0 \\ \lambda_b & \lambda_b & M_b & 0 & 0 & 0 \\ 0 & 0 & 0 & \mu_b & 0 & 0 \\ 0 & 0 & 0 & 0 & \mu_b & 0 \\ 0 & 0 & 0 & 0 & 0 & \mu_b \end{bmatrix}$$

$\mathbf{C}^{\mathrm{T}}$ represents the stiffness matrix perturbation caused by inclined fractures, the specific elements of which are denoted as:

$$\begin{aligned}
C_{11} &= -\left(\cos^2\xi_1\chi_b - \sin^2\xi_1\right)^2 M_b\delta_{N1}^{\mathrm{tilted}} - \sin^2 2\xi_1\mu_b\delta_{T1}^{\mathrm{tilted}}, \\
C_{12} &= -\left(\chi_b\cos^2\xi_1 + \sin^2\xi_1\right)\lambda_b\delta_{N1}^{\mathrm{tilted}}, \\
C_{13} &= -\left[\frac{1}{4}\sin^2 2\xi_1(1-\chi_b)^2 + \chi_b\right]M_b\delta_{N1}^{\mathrm{tilted}} + \sin^2 2\theta_1\mu_b\delta_{T1}^{\mathrm{tilted}},
\end{aligned}$$

$$\begin{aligned}
C_{15} &= \sin 2\theta_1\left(\chi_b\cos^2\xi_1 + \sin^2\xi_1\right)\delta_{N1}^{\mathrm{tilted}}\mu_b + \sin 2\theta_1\cos 2\theta_1\mu_b\delta_{T1}^{\mathrm{tilted}}, \\
C_{22} &= -\chi_b^2 M_b\delta_{N1}^{\mathrm{tilted}}, \\
C_{23} &= -\left(\sin^2\xi_1\chi_b + \cos^2\xi_1\right)\lambda_b\delta_{N1}^{\mathrm{tilted}}, \\
C_{25} &= \sin 2\xi_1\chi_b\mu_b\delta_{N1}^{\mathrm{tilted}}, \\
C_{33} &= -\left(\sin^2\xi_1\chi_b + \cos^2\xi_1\right)^2 M_b\delta_{N1}^{\mathrm{tilted}} - \sin^2 2\xi_1\mu_b\delta_{T1}^{\mathrm{tilted}}, \\
C_{35} &= \left(\chi_b\sin^2\xi_1 + \cos^2\xi_1\right)\sin 2\xi_1\mu_b\delta_{N1}^{\mathrm{tilted}} - \sin 2\xi_1\cos 2\theta_1\mu_b\delta_{T1}^{\mathrm{tilted}}, \\
C_{44} &= -\cos^2\xi_1\mu_b\delta_{T1}^{\mathrm{tilted}}, \\
C_{46} &= \frac{1}{2}\sin 2\xi_1\mu_b\delta_{T1}^{\mathrm{tilted}}, \\
C_{55} &= -\frac{1}{4}(1-\chi_b)^2\sin^2 2\xi_1 M_b\delta_{N1}^{\mathrm{tilted}} - \cos^2 2\xi_1\mu_b\delta_{T1}^{\mathrm{tilted}}, \\
C_{66} &= -\sin^2\xi_1\mu_b\delta_{T1}^{\mathrm{tilted}}.
\end{aligned}$$

where, λ_b and μ_b refers to the Lame coefficient of the background isotropic medium, $M_b = \lambda_b + 2\mu_b$ is the longitudinal wave modulus. $\chi_b = \lambda_b/\mu_b$ is the ratio of the Lame coefficient to provide a more concise representation of the stiffness matrix perturbation caused by the fracture. ξ_1 indicates the degree of inclination of the fracture, and $\delta_{N1}^{\mathrm{titled}}$ is normal weakness, $\delta_{T1}^{\mathrm{titled}}$ is tangential weakness. Which are dimensionless fracture parameters used to express the nature of the fracture.

When two sets of inclined fractures are introduced into an isotropic medium, the resulting composite material can be represented as a monoclinic medium. The physical properties of such a monoclinic medium are closely related to the physical properties of the background rocks as well as the physical properties of the two groups of fractures. To reduce the difficulty of finding the physical properties of this monoclinic medium, we assume that the effects of the two sets of fractures are independent of one another, based on the principle of perturbation, thereby allowing us to disregard any potential interactions between the two fracture sets. Consequently, the resulting stiffness matrix of the medium embedded in two sets of inclined fractures can be expressed as follows:

$$
\mathbf{C}^{\mathrm{Mono}}=\mathbf{C}^{\mathrm{Iso}}+\mathbf{C}^{\mathrm{f1}}+\mathbf{C}^{\mathrm{f2}}
=\begin{bmatrix}
C_{11} & C_{12} & C_{13} & 0 & C_{15} & 0\\
C_{12} & C_{22} & C_{23} & 0 & C_{25} & 0\\
C_{13} & C_{23} & C_{33} & 0 & C_{35} & 0\\
0 & 0 & 0 & C_{44} & 0 & C_{46}\\
C_{15} & C_{25} & C_{35} & 0 & C_{55} & 0\\
0 & 0 & 0 & C_{46} & 0 & C_{66}
\end{bmatrix} \tag{2}
$$

This stiffness matrix element is in the form of

Based on Shaw and Sen (2004) theory of reflection coefficient equation derivation based on seismic scattering:

$$
R_{\mathrm{PP}}(\theta,\varphi)=\frac{1}{4\rho_{\mathrm{b}}\cos^2\theta}\left(\Delta\rho_{\mathrm{b}}\chi+\Delta\mathbf{C}\boldsymbol{\eta}\right) \tag{4}
$$

where ρ_{b} representing the density of the medium, χ is a parameter related to the polarization vector, $\boldsymbol{\eta}$ is a matrix of 6 rows and 6 columns, the angle of incidence and azimuth are closely related to its elements. Utilizing the aforementioned theoretical framework,

$$
\begin{aligned}
C_{11}&=M_{\mathrm{b}}-\left(\cos^2\xi_1\chi_{\mathrm{b}}-\sin^2\xi_1\right)^2M_{\mathrm{b}}\delta_{\mathrm{N1}}^{\mathrm{tilted}}-\sin^2 2\xi_1\mu_{\mathrm{b}}\delta_{\mathrm{T1}}^{\mathrm{tilted}}\\
&\quad-\left(\cos^2\xi_2\chi_{\mathrm{b}}-\sin^2\xi_2\right)^2M_{\mathrm{b}}\delta_{\mathrm{N2}}^{\mathrm{tilted}}-\sin^2 2\xi_2\mu_{\mathrm{b}}\delta_{\mathrm{T2}}^{\mathrm{tilted}},\\
C_{12}&=\lambda_{\mathrm{b}}-\left(\chi_b\cos^2\xi_1+\sin^2\xi_1\right)\lambda_{\mathrm{b}}\delta_{\mathrm{N1}}^{\mathrm{tilted}}-\left(\chi_b\cos^2\xi_2+\sin^2\xi_2\right)\lambda_{\mathrm{b}}\delta_{\mathrm{N2}}^{\mathrm{tilted}},\\
C_{13}&=\lambda_{\mathrm{b}}-\left[\frac{1}{4}\sin^2 2\xi_1(1-\chi_{\mathrm{b}})^2+\chi_{\mathrm{b}}\right]M_{\mathrm{b}}\delta_{\mathrm{N1}}^{\mathrm{tilted}}+\sin^2 2\xi_1\mu_{\mathrm{b}}\delta_{\mathrm{T1}}^{\mathrm{tilted}}\\
&\quad-\left[\frac{1}{4}\sin^2 2\xi_2(1-\chi_{\mathrm{b}})^2+\chi_{\mathrm{b}}\right]M_{\mathrm{b}}\delta_{\mathrm{N2}}^{\mathrm{tilted}}+\sin^2 2\xi_2\mu_{\mathrm{b}}\delta_{\mathrm{T1}}^{\mathrm{tilted}},\\
C_{15}&=\sin 2\xi_1\left(\chi_{\mathrm{b}}\cos^2\xi_1+\sin^2\xi_1\right)\delta_{\mathrm{N1}}^{\mathrm{tilted}}\mu_{\mathrm{b}}+\sin 2\xi_1\cos 2\xi_1\mu_{\mathrm{b}}\delta_{\mathrm{T1}}^{\mathrm{tilted}}\\
&\quad+\sin 2\xi_2\left(\chi_{\mathrm{b}}\cos^2\xi_2+\sin^2\xi_2\right)\delta_{\mathrm{N2}}^{\mathrm{tilted}}\mu_{\mathrm{b}}+\sin 2\xi_2\cos 2\xi_2\mu_{\mathrm{b}}\delta_{\mathrm{T2}}^{\mathrm{tilted}},\\
C_{22}&=M_{\mathrm{b}}-\chi_{\mathrm{b}}^2M_{\mathrm{b}}\delta_{\mathrm{N1}}^{\mathrm{tilted}}-\chi_{\mathrm{b}}^2M_{\mathrm{b}}\delta_{\mathrm{N2}}^{\mathrm{tilted}},\\
C_{23}&=\lambda_{\mathrm{b}}-\left(\sin^2\xi_1\chi_{\mathrm{b}}+\cos^2\xi_1\right)\lambda_{\mathrm{b}}\delta_{\mathrm{N1}}^{\mathrm{tilted}}-\left(\sin^2\xi_2\chi_{\mathrm{b}}+\cos^2\xi_2\right)\lambda_{\mathrm{b}}\delta_{\mathrm{N2}}^{\mathrm{tilted}},\\
C_{25}&=\sin 2\xi_1\chi_{\mathrm{b}}\mu_{\mathrm{b}}\delta_{\mathrm{N1}}^{\mathrm{tilted}}+\sin 2\xi_2\chi_{\mathrm{b}}\mu_{\mathrm{b}}\delta_{\mathrm{N2}}^{\mathrm{tilted}},\\
C_{33}&=M_{\mathrm{b}}-\left(\sin^2\xi_1\chi_{\mathrm{b}}+\cos^2\xi_1\right)^2M_{\mathrm{b}}\delta_{\mathrm{N1}}^{\mathrm{tilted}}-\sin^2 2\xi_1\mu_{\mathrm{b}}\delta_{\mathrm{T1}}^{\mathrm{tilted}}\\
&\quad-\left(\sin^2\xi_2\chi_{\mathrm{b}}+\cos^2\xi_2\right)^2M_{\mathrm{b}}\delta_{\mathrm{N2}}^{\mathrm{tilted}}-\sin^2 2\xi_2\mu_{\mathrm{b}}\delta_{\mathrm{T2}}^{\mathrm{tilted}},\\
C_{35}&=\left(\chi_{\mathrm{b}}\sin^2\xi_1+\cos^2\xi_1\right)\sin 2\xi_1\mu_{\mathrm{b}}\delta_{\mathrm{N1}}^{\mathrm{tilted}}-\sin 2\xi_1\cos 2\xi_1\mu_{\mathrm{b}}\delta_{\mathrm{T1}}^{\mathrm{tilted}}\\
&\quad\left(\chi_{\mathrm{b}}\sin^2\xi_2+\cos^2\xi_2\right)\sin 2\xi_2\mu_{\mathrm{b}}\delta_{\mathrm{N2}}^{\mathrm{tilted}}-\sin 2\xi_2\cos 2\xi_2\mu_{\mathrm{b}}\delta_{\mathrm{T2}}^{\mathrm{tilted}},\\
C_{44}&=\mu_{\mathrm{b}}-\cos^2\xi_1\mu_{\mathrm{b}}\delta_{\mathrm{T1}}^{\mathrm{tilted}}-\cos^2\xi_2\mu_{\mathrm{b}}\delta_{\mathrm{T2}}^{\mathrm{tilted}},\\
C_{46}&=\frac{1}{2}\sin 2\xi_1\mu_{\mathrm{b}}\delta_{\mathrm{T1}}^{\mathrm{tilted}}+\frac{1}{2}\sin 2\xi_2\mu_{\mathrm{b}}\delta_{\mathrm{T2}}^{\mathrm{tilted}},
\end{aligned}
$$

$$
\begin{aligned}
C_{55}&=\mu_{\mathrm{b}}-\frac{1}{4}(1-\chi_{\mathrm{b}})^2\sin^2 2\xi_1M_{\mathrm{b}}\delta_{\mathrm{N1}}^{\mathrm{tilted}}-\cos^2 2\xi_1\mu_{\mathrm{b}}\delta_{\mathrm{T1}}^{\mathrm{tilted}}\\
&\quad-\frac{1}{4}(1-\chi_{\mathrm{b}})^2\sin^2 2\xi_2M_{\mathrm{b}}\delta_{\mathrm{N2}}^{\mathrm{tilted}}-\cos^2 2\xi_2\mu_{\mathrm{b}}\delta_{\mathrm{T2}}^{\mathrm{tilted}},\\
C_{66}&=\mu_{\mathrm{b}}-\sin^2\xi_1\mu_{\mathrm{b}}\delta_{\mathrm{T1}}^{\mathrm{tilted}}-\sin^2\xi_2\mu_{\mathrm{b}}\delta_{\mathrm{T2}}^{\mathrm{tilted}}.
\end{aligned}
$$

Then, based on the weak anisotropy, we use Psencik's theory to derive the perturbation matrix:

$$
\Delta\mathbf{C}_{\mathrm{Mono}}\approx\begin{bmatrix}
\Delta C_{11} & \Delta C_{12} & \Delta C_{13} & 0 & \Delta C_{15} & 0\\
\Delta C_{12} & \Delta C_{22} & \Delta C_{23} & 0 & \Delta C_{25} & 0\\
\Delta C_{13} & \Delta C_{23} & \Delta C_{33} & 0 & \Delta C_{35} & 0\\
0 & 0 & 0 & \Delta C_{44} & 0 & \Delta C_{46}\\
\Delta C_{15} & \Delta C_{25} & \Delta C_{35} & 0 & \Delta C_{55} & 0\\
0 & 0 & 0 & \Delta C_{46} & 0 & \Delta C_{66}
\end{bmatrix} \tag{3}
$$

we derive the reflection coefficient equation for linearized PP waves in the medium under investigation. Following this derivation, we apply the second-order approximation to obtain the final reflection coefficient equation as follows:

$$
\begin{aligned}
R_{\mathrm{pp}}(\theta,\varphi)=&\,a(\theta)\frac{\Delta M_{\mathrm{b}}}{M_{\mathrm{b}}}+b(\theta)\frac{\Delta\mu_{\mathrm{b}}}{\mu_{\mathrm{b}}}+d(\theta,\varphi)\Delta\delta_{\mathrm{N1}}^{\mathrm{tilted}}\\
&+f(\theta,\varphi)\Delta\delta_{\mathrm{N2}}^{\mathrm{tilted}}+e(\theta,\varphi)\Delta\delta_{\mathrm{T1}}^{\mathrm{tilted}}+g(\theta,\varphi)\Delta\delta_{\mathrm{T2}}^{\mathrm{tilted}}
\end{aligned} \tag{5}
$$

where

$$
a(\theta)=\frac{\sec^2\theta}{4},\ b(\theta)=-2g\sin^2\theta,
$$

$$d(\theta,\varphi)=\begin{bmatrix} -\frac{1}{4}\left(1-2g\sin^2\xi_1\right)^2+ \\ \left(g-2g\sin^2\xi_1+g^2\sin^4\xi_1-\frac{1}{4}\right)\sin^2\theta+ \\ \left(\frac{1}{2}g^2\sin^2 2\xi_1+g^2\sin^2\xi_1\right)\sin^2\theta\cos^2\varphi \end{bmatrix}$$

$$f(\theta,\varphi)=\begin{bmatrix} -\frac{1}{4}\left(1-2g\sin^2\xi_2\right)^2+ \\ \left(g-2g\sin^2\xi_2+g^2\sin^4\xi_2-\frac{1}{4}\right)\sin^2\theta+ \\ \left(\frac{1}{2}g^2\sin^2 2\xi_2+g^2\sin^2\xi_2\right)\sin^2\theta\cos^2\varphi \end{bmatrix}$$

$$e(\theta,\varphi)=\begin{bmatrix} \left(-\frac{1}{4}g\sin^2 2\xi_1+\left(g\cos^2\xi_1+\frac{1}{4}g\sin^2 2\xi_1\right)\sin^2\theta\right. \\ \left.+\left(g\cos^2 2\xi_1+\frac{1}{2}g\sin^2 2\xi_1-g\cos^2\xi_1\right)\sin^2\theta\cos^2\varphi\right. \end{bmatrix}$$

$$g(\theta,\varphi)=\begin{bmatrix} \left(-\frac{1}{4}g\sin^2 2\xi_2+\left(g\cos^2\xi_2+\frac{1}{4}g\sin^2 2\xi_2\right)\sin^2\theta\right. \\ \left.+\left(g\cos^2 2\xi_2+\frac{1}{2}g\sin^2 2\xi_2-g\cos^2\xi_2\right)\sin^2\theta\cos^2\varphi\right. \end{bmatrix}$$

When the inclination angles of the two sets of inclined fractures are identical, the two sets effectively merge into a single set, resulting in a monoclinic medium that simplifies to a TTI medium. In this case, the reflection coefficient equation aligns with the expression derived by Pan et al. (2021). Additionally, if the inclination angles of the two fracture sets are either 0° or 90°, the monoclinic medium transitions into either a VTI or an HTI medium. The reflection coefficient equation for HTI media is consistent with those obtained by Pan et al. (2021) and Chen et al. (2017). Furthermore, if one set of fractures has an inclination angle of 0° and the other set is inclined at 90°, the monoclinic medium reduces to an Orthorhombic Anisotropy (OA) medium, and the simplified reflection coefficient equation matches the result derived by Zhang et al. (2020). These observations confirm the validity of the derived reflection coefficient equation. Appendix 1 shows the detailed proof process for the above.

Due to the extensive number of parameters required for inversion in Eq. (5), the inversion results are prone to increased instability and multiple solutions. To address this issue and get the inversion results more stably, we utilize the relationship between fracture weakness and fracture density established by Bakulin et al. (2000a). Specifically, Bakulin indicates that for dry fractures, the relationship between normal weakness and tangential weakness is given by

$$\delta_\mathrm{N}=\frac{4e}{3g(1-g)};\ \delta_\mathrm{T}=\frac{16e}{3(3-2g)} \tag{6}$$

where, $g=V_s^2/V_p^2$ is the square ratio of S-wave velocity to P-wave velocity, Substituting Eq. (6) into Eq. (5) yields:

$$R_\mathrm{pp}(\theta,\varphi)=a(\theta)\frac{\Delta M_\mathrm{b}}{M_\mathrm{b}}+b(\theta)\frac{\Delta\mu_\mathrm{b}}{\mu_\mathrm{b}}+h(\theta,\varphi)\Delta e1+i(\theta,\varphi)\Delta e2 \tag{7}$$

where

$$h(\theta,\varphi)=\frac{\left(1-2g\sin^2\xi_1\right)^2}{3g(1-g)}-\frac{4g\sin^2 2\xi_1}{3(3-2g)} +\begin{bmatrix}\frac{\left(1-2g\sin^2\xi_1\right)^2-2(1-2g)\left(1-2g\sin^2\xi_1\right)}{3g(1-g)}+ \\ \frac{16g\cos^2\xi_1+4g\sin^2\xi_1-2g\sin^2\xi_1}{3(3-2g)}\end{bmatrix}\sin^2\theta +\begin{bmatrix}\frac{2(1-2g)\left(1-2g\sin^2\xi_1\right)+2g^2\sin^2\xi_1+4g-2}{3g(1-g)}+ \\ \frac{16g\cos^2 2\xi_1+8g\sin^2 2\xi_1-16g\cos^2\xi_1}{3(3-2g)}\end{bmatrix}\sin^2\theta\cos^2\varphi$$

$$i(\theta,\varphi)=\frac{\left(1-2g\sin^2\xi_2\right)^2}{3g(1-g)}-\frac{4g\sin^2 2\xi_2}{3(3-2g)} +\begin{bmatrix}\frac{\left(1-2g\sin^2\xi_2\right)^2-2(1-2g)\left(1-2g\sin^2\xi_2\right)}{3g(1-g)}+ \\ \frac{16g\cos^2\xi_2+4g\sin^2\xi_2-2g\sin^2\xi_2}{3(3-2g)}\end{bmatrix}\sin^2\theta +\begin{bmatrix}\frac{2(1-2g)\left(1-2g\sin^2\xi_2\right)+2g^2\sin^2\xi_2+4g-2}{3g(1-g)}+ \\ \frac{16g\cos^2 2\xi_2+8g\sin^2 2\xi_2-16g\cos^2\xi_2}{3(3-2g)}\end{bmatrix}\sin^2\theta\cos^2\varphi$$

The simplified reflection coefficient equation has only four parameters to be inverted, which improves the stability of the inversion process.

2.2. Reflection coefficient equation analysis

The derived reflection coefficient equation is influenced by both the intrinsic properties of the formation and fractures, as well as the incidence angle and azimuth angle. To investigate how the reflection coefficient varies with these parameters, we employ a simplified model for forward modeling of the reflection coefficient equation. The model's detailed parameters are provided in Table 1.

Fig. 1 illustrates the effects of incidence angle, azimuth angle, and fracture dip on the reflection coefficient. As can be seen from Fig. 1, when the dip of both fracture sets is zero, the reflection coefficient depends solely on the incidence angle. However, with a nonzero dip in any fracture set, the reflection coefficient is no longer independent of the azimuth. Moreover, as the fracture dip rises, the reflection coefficient demonstrates more noticeable fluctuations in response to changes in the azimuth angle.

The elastic parameters of the isotropic background and the fracture density of the two groups of fractures directly affect the value of the reflection coefficient. To identify optimal inversion parameters, initially, we determined the range of disturbance values for the parameters based on data from multiple wells across

Table 1
Two-layer model parameter values.

Layer	M_b, GPa	μ_b, GPa	$e1$	$e2$
Upper	1.85	1.15	0.13	0.010
Lower	2.48	1.32	0.31	0.175

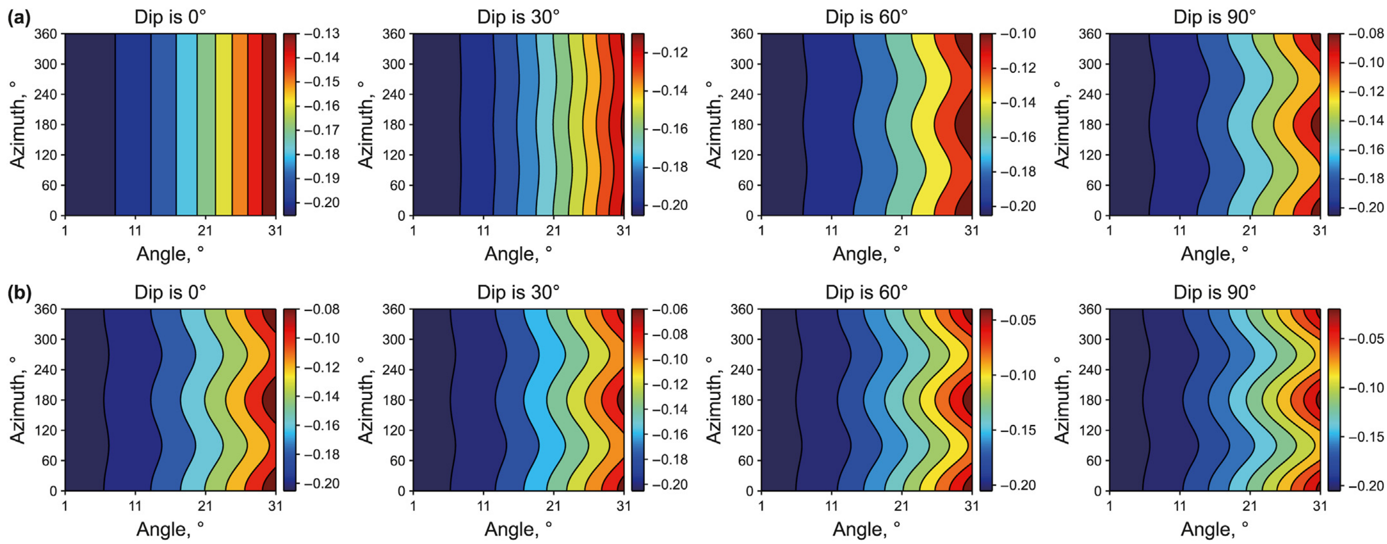

Fig. 1. Reflection coefficient variation with incidence angle, azimuth angle, and fracture dip. **(a)** The dip of the first set of fractures is 0°. **(b)** The dip of the first set of fractures is 45°.

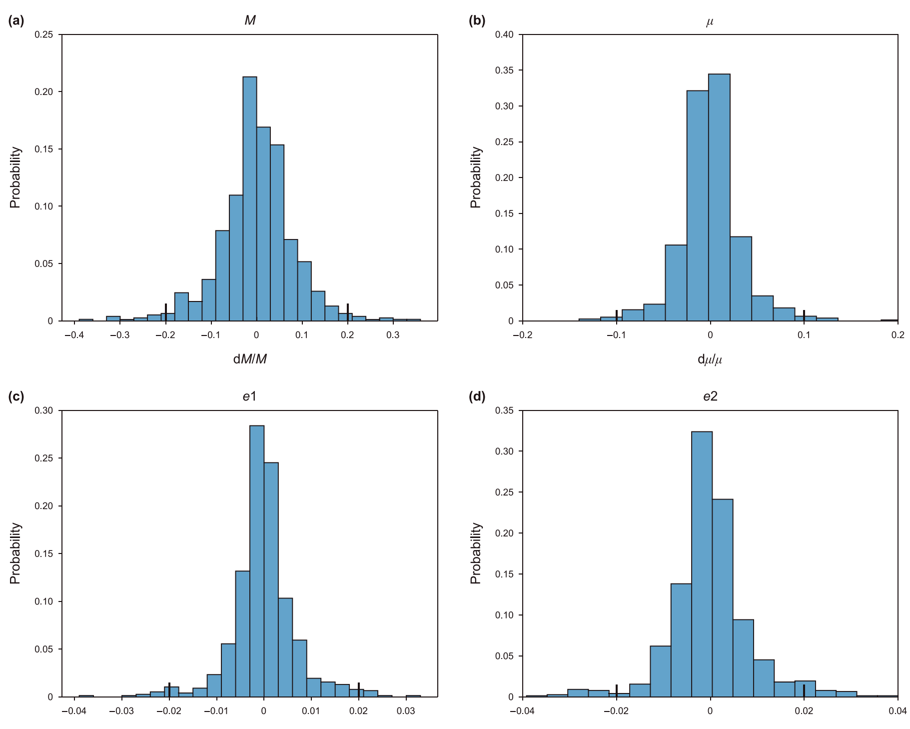

Fig. 2. The perturbation distribution of the parameters to be inverted. **(a)**M_b, **(b)**μ_b, **(c)**$e1$, **(d)**$e2$.

different work areas. Subsequently, we selected several representative values from these statistical results to assess how small perturbations in the parameters influence changes in the reflection coefficient. The results are presented in Fig. 2.

The parameter perturbation satisfies a normal distribution with a mean of 0 from Fig. 2, we choose a 95% confidence interval of the normal distribution to study the contribution of longitudinal wave modulus M_b, shear wave modulus μ_b and fracture density $e1, e2$ to the reflection coefficient to determine better inversion parameters.

Since we assume that the two sets of fractures are not related to each other, studying the effects of both sets of fractures can be simplified to examining the effects of a single set of fractures. We set the inclination angle of the two groups of fractures to the same degree to investigate how the inclination angle affects the reflection coefficient. Fig. 3 illustrates that the longitudinal wave modulus (M_b) contributes the most to the reflection coefficient equation, and its contribution rate is more than 55%. As the inclination angle of the fracture increases, the contribution of the

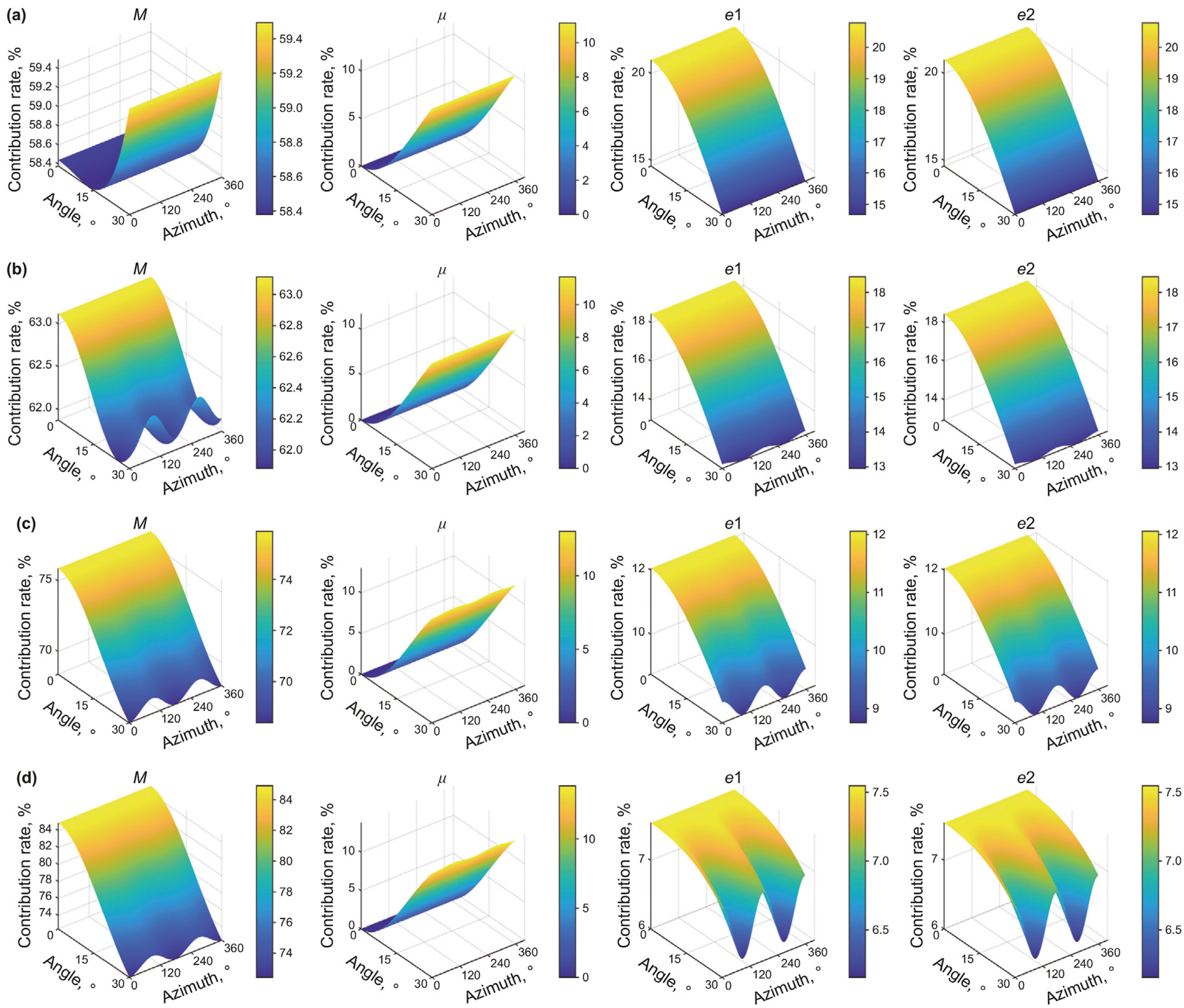

Fig. 3. Various parameters contribute to the reflection coefficient as the incidence and azimuth angles change. **(a)** The dip of both groups of fractures is 0°. **(b)** The dip of both groups of fractures is 30°. **(c)** The dip of both groups of fractures is 60°. **(d)** The dip of both groups of fractures is 90°.

fracture density to the reflection coefficient decreases gradually. When the inclination angle is nonzero, the contributions of the background elastic parameters, and fracture density to the reflection coefficient exhibit azimuth-dependent variations. Therefore, seismic data with small incidence angles and azimuth angles of 0°, 180°, and 360° are recommended for achieving more accurate inversion of fracture parameters.

2.3. Derivation of the inversion equation for azimuth elastic impedance

Azimuth elastic impedance inversion has proved to be an effective and stable inversion method. The azimuth anisotropy elastic impedance equation in Eq. (7) can be written as:

$$L_{EI}(\theta,\varphi)=a(\theta)L_{M_\mathrm{b}}+b(\theta)L_{\mu_\mathrm{b}}+h(\theta,\varphi)e1+i(\theta,\varphi)e2 \tag{8}$$

with $L_{EI}(\theta,\ \varphi)\ =\ \ln(EI(\theta,\ \varphi)/EI_0)$, $L_{M_\mathrm{b}}\ =\ \ln\left(M_\mathrm{b}(\theta)/M_\mathrm{b}^0\right)$, $L_{\mu_\mathrm{b}}\ =\ \ln\left(\mu_\mathrm{b}(\theta)/\mu_\mathrm{b}^0\right)$

When the seismic data has L incidence angles, M azimuth angles, and N time sampling points, the inversion equation can be written as:

$$\mathbf{d}_{NML\times 1}=\mathbf{G}_{NML\times 4N}\mathbf{m}_{4N\times 1} \tag{9}$$

where, $\mathbf{d}$ is the seismic data and $\mathbf{d}\ =\left[L_{EI}(\theta_1,\varphi_1)\quad\cdots\quad L_{EI}(\theta_L,\varphi_M)\right]^\mathrm{T}$, $\mathbf{G}$ is the observation matrix with

$$\mathbf{G}=\begin{bmatrix}\mathbf{W}_{\theta_1}\mathbf{K}_{M_\mathrm{b}}(\theta_1) & \mathbf{W}_{\theta_1}\mathbf{K}_{\mu_\mathrm{b}}(\theta_1) & \mathbf{W}_{\theta_1}\mathbf{K}_{e1}(\theta_1,\varphi_1) & \mathbf{W}_{\theta_1}\mathbf{K}_{e2}(\theta_1,\varphi_1)\\ \vdots & \vdots & \vdots & \vdots\\ \mathbf{W}_{\theta_L}\mathbf{K}_{M_\mathrm{b}}(\theta_\mathrm{L}) & \mathbf{W}_{\theta_L}\mathbf{K}_{\mu_\mathrm{b}}(\theta_L) & \mathbf{W}_{\theta_L}\mathbf{K}_{e1}(\theta_L,\varphi_M) & \mathbf{W}_{\theta_L}\mathbf{K}_{e2}(\theta_L,\varphi_M)\end{bmatrix}$$

where $\mathbf{W}_{\theta_i}$ is the wavelet matrix, which is in the form of

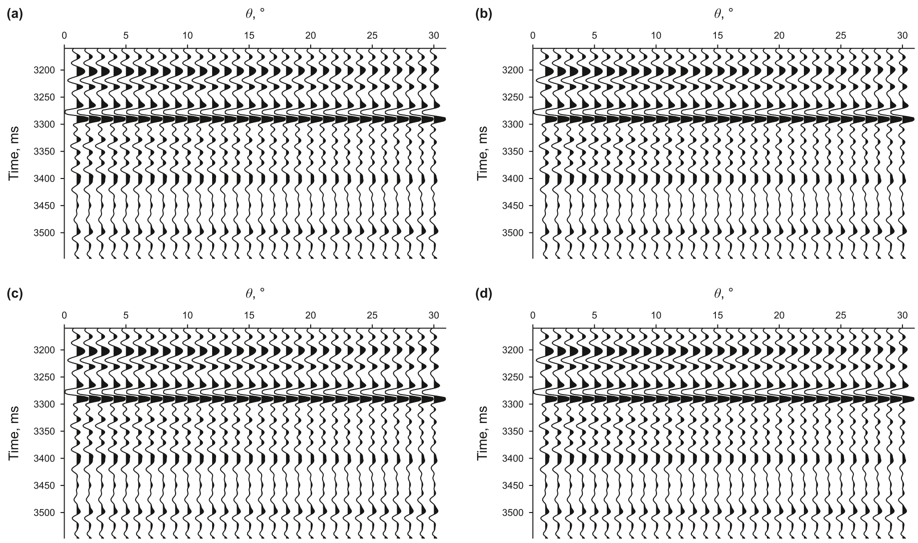

Fig. 4. Noise-free synthetic seismic record**.** Azimuths are 60° **(a)**, 120° **(b)**, 180°**(c)**, 240° **(d).**

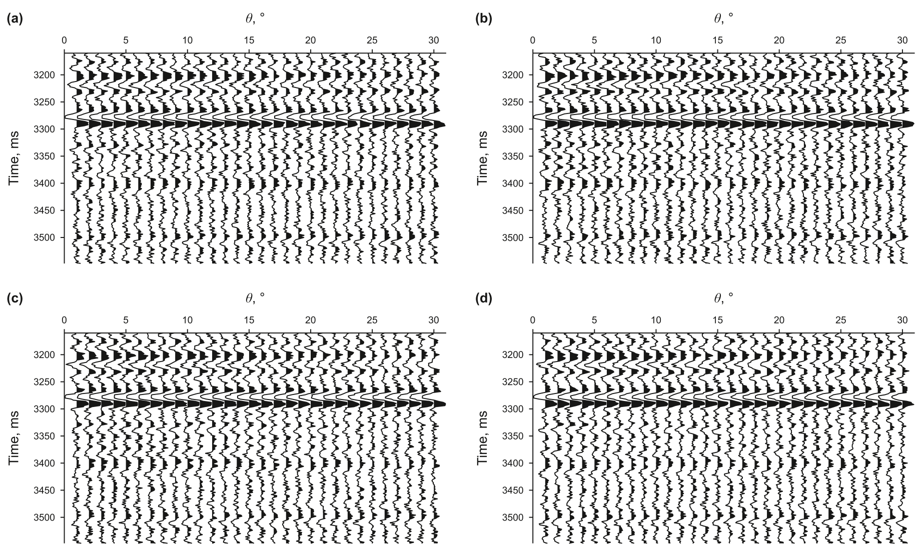

Fig. 5. Synthetic seismic record with $S/N = 2$. Azimuths are 60° **(a)**, 120° **(b)**, 180°**(c)**, 240° **(d).**

$$\mathbf{W}_{\theta_i} = \begin{bmatrix} w_{\theta_i}^1 & 0 & 0 & \cdots \\ w_{\theta_i}^2 & w_{\theta_i}^1 & 0 & \ddots \\ w_{\theta_i}^3 & w_{\theta_i}^2 & w_{\theta_i}^1 & \ddots \\ \vdots & \ddots & \ddots & \ddots \end{bmatrix}$$

and

$$\mathbf{K}_{M_\mathrm{b}}(\theta_1) = \begin{bmatrix} a(\theta_1) & 0 & \cdots & 0 \\ 0 & a(\theta_1) & \cdots & 0 \\ \vdots & \vdots & \ddots & \vdots \\ 0 & 0 & 0 & a(\theta_1) \end{bmatrix}_{N\times N},$$

$$\mathbf{K}_{\mu_\mathrm{b}}(\theta_1) = \begin{bmatrix} b(\theta_1) & 0 & \cdots & 0 \\ 0 & b(\theta_1) & \cdots & 0 \\ \vdots & \vdots & \ddots & \vdots \\ 0 & 0 & 0 & b(\theta_1) \end{bmatrix}_{N\times N},$$

$$\mathbf{K}_{e1}(\theta_1,\varphi_1) = \begin{bmatrix} h(\theta_1,\varphi_1) & 0 & \cdots & 0 \\ 0 & h(\theta_1,\varphi_1) & \cdots & 0 \\ \vdots & \vdots & \ddots & \vdots \\ 0 & 0 & 0 & h(\theta_1,\varphi_1) \end{bmatrix}_{N\times N},$$

$$\mathbf{K}_{e2}(\theta_1,\varphi_1) = \begin{bmatrix} i(\theta_1,\varphi_1) & 0 & \cdots & 0 \\ 0 & i(\theta_1,\varphi_1) & \cdots & 0 \\ \vdots & \vdots & \ddots & \vdots \\ 0 & 0 & 0 & i(\theta_1,\varphi_1) \end{bmatrix}_{N\times N}$$

$\mathbf{m}$ is the parameter to be inverted, and its specific form is $\mathbf{m} = [\mathbf{L}_M \quad \mathbf{L}_\mu \quad \mathbf{e1} \quad \mathbf{e2}]^\mathrm{T}_{4K\times 1}$, and

$$\mathbf{L}_{M_\mathrm{b}} = [\ln M_\mathrm{b}(t_1) \quad \cdots \quad \ln M_\mathrm{b}(t_N)]^\mathrm{T},\ \mathbf{L}_{\mu_\mathrm{b}} = [\ln \mu_\mathrm{b}(t_1) \quad \cdots \quad \ln \mu_\mathrm{b}(t_N)]^\mathrm{T},\ \mathbf{e1} = [e1(t_1) \quad \cdots \quad e1(t_N)]^\mathrm{T},\ \mathbf{e2} = [e2(t_1) \quad \cdots \quad e2(t_N)]^\mathrm{T}$$

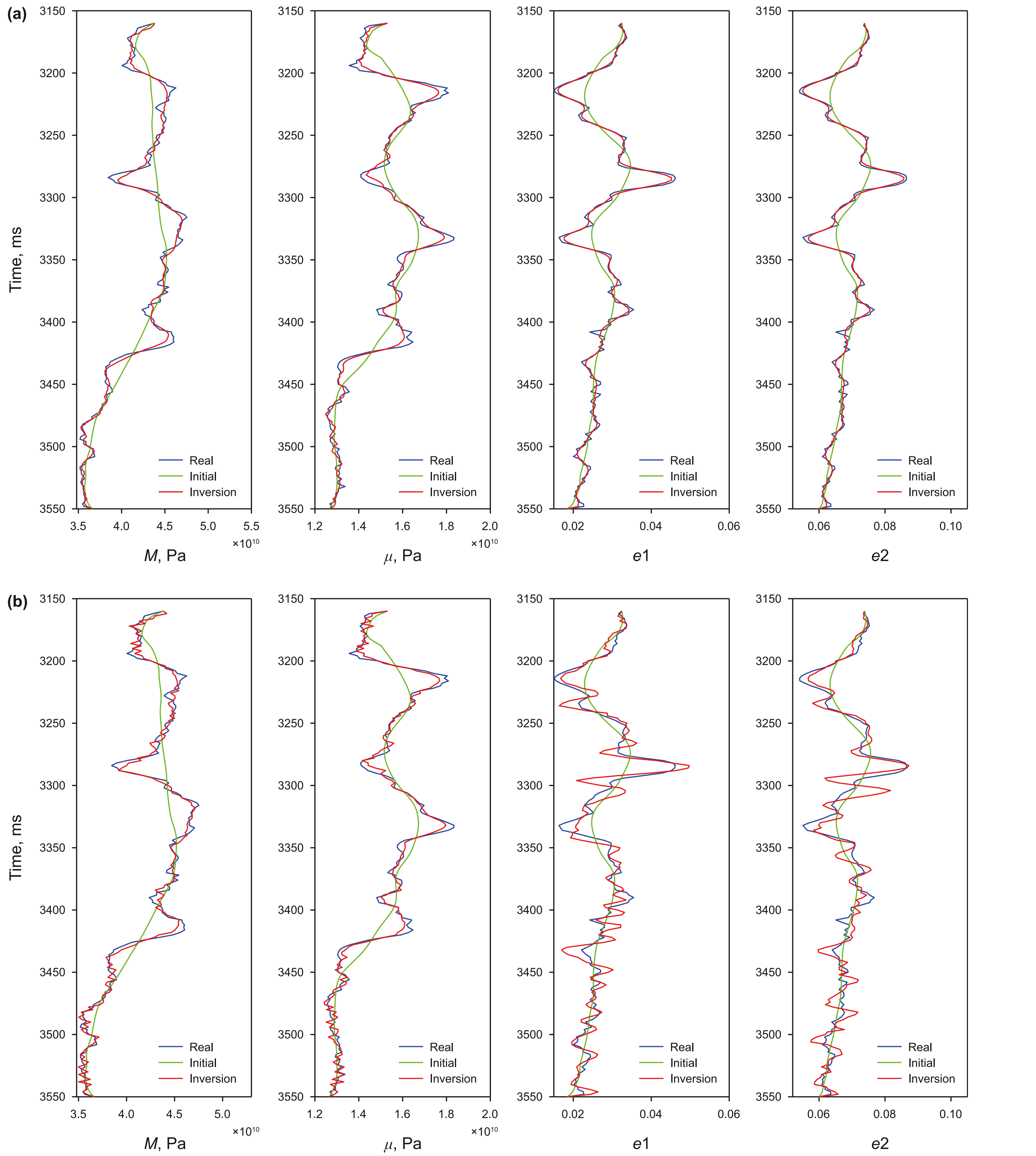

Fig. 6. Noise-free inversion results. **(a)** Four parameter inversion results, **(b)** six parameter indirect inversion results.

Inversion results may experience interference in accuracy and stability due to the correlation of model parameters. To address this, the decorrelation method is applied to the model parameters, along with a low-frequency constraint to enhance inversion stability. The final expression for the inverted equation is as follows:

$$F(m') = (\mathbf{d} - \mathbf{G}'\mathbf{m}')^{\mathrm{T}}(\mathbf{d} - \mathbf{G}'\mathbf{m}') + 2\nu_n^2 \sum_{i=1}^{4N} \ln\left(1 + m_i^2 \Big/ \nu_m^2\right) + \mathbf{\Lambda} \tag{10}$$

where

$$\mathbf{\Lambda} = \gamma_{M_b}\left(\eta_{M_b} - \mathbf{P}L'_{M_b}\right)^{\mathrm{T}}\left(\eta_{M_b} - \mathbf{P}L'_{M_b}\right) + \gamma_{\mu_b}\left(\eta_{\mu_b} - \mathbf{P}L'_{\mu_b}\right)^{\mathrm{T}}\left(\eta_{\mu_b} - \mathbf{P}L'_{\mu_b}\right) + \gamma_{e1}\left(\eta_{e1} - \mathbf{P}L'_{e1}\right)^{\mathrm{T}}\left(\eta_{e1} - \mathbf{P}L'_{e1}\right) + \gamma_{e1}\left(\eta_{e2} - \mathbf{P}L'_{e2}\right)^{\mathrm{T}}\left(\eta_{e2} - \mathbf{P}L'_{e2}\right)$$

$$\eta_{M_b} = 1\Big/2 \times \ln\left(L_{M_b}\Big/L_{M_b^0}\right), \eta_{\mu_b} = 1\Big/2 \times \ln\left(L_{\mu_b}\Big/L_{\mu_b^0}\right),$$
$$\eta_{e1} = 1\Big/2 \times \ln\left(L_{e1}\Big/L_{e1^0}\right), \eta_{e2} = 1\Big/2 \times \ln\left(L_{e2}\Big/L_{e2^0}\right)$$

where, γ_{M_b}, γ_{μ_b}, γ_{e1}, γ_{e2} represents the constraint coefficient of the corresponding parameter, and $L_{M_b^0}$, $L_{\mu_b^0}$, L_{e1^0}, L_{e2^0} represents the

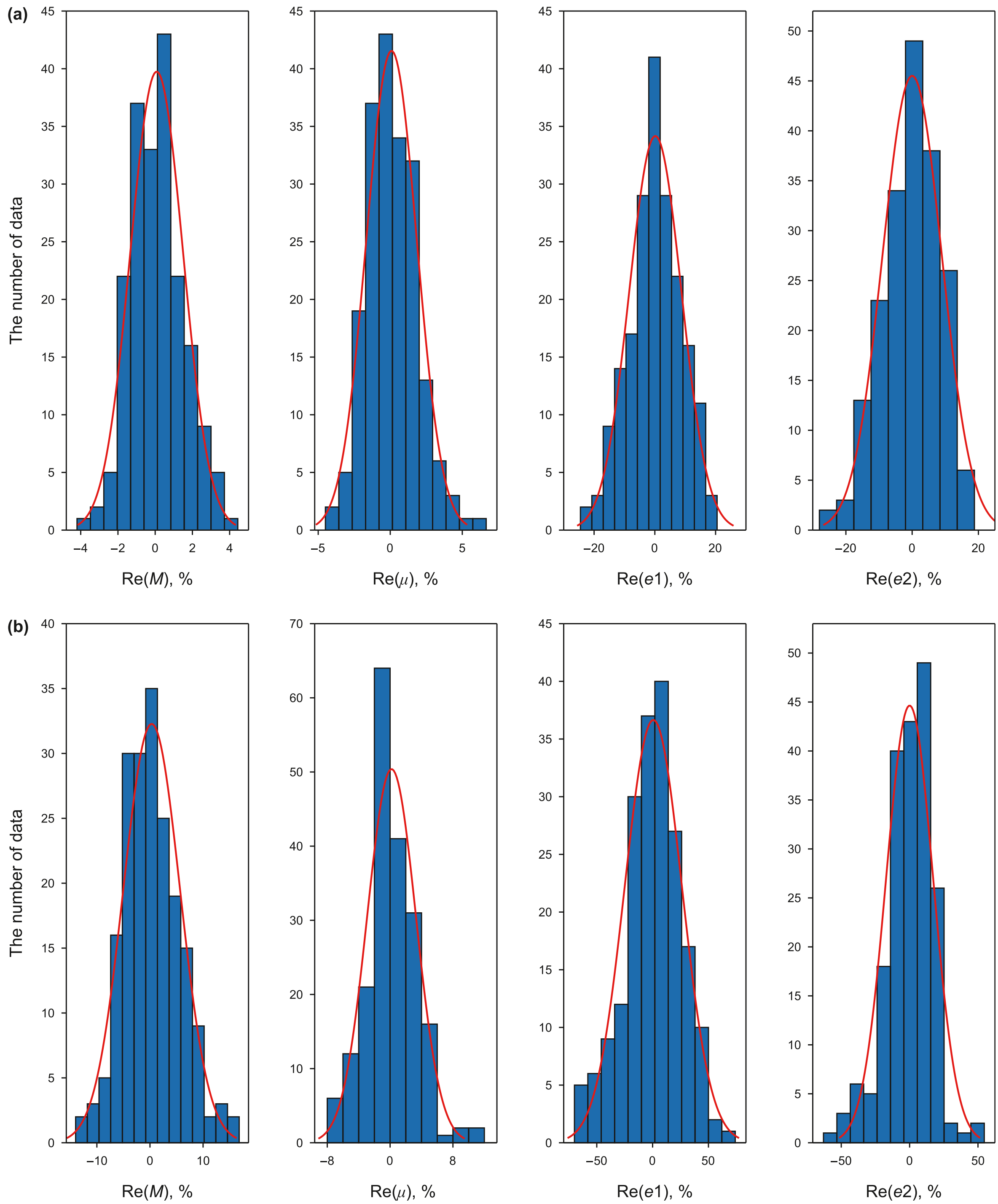

Fig. 7. The error of Noise-free inversion result (Re is relative error)**. (a)** Four parameter inversion error; **(b)** six parameter indirect inversion error.

initial value of the corresponding parameter. The repeated weighted least squares method is employed to solve Eq. (10), resulting in the obtaination of the background isotropy parameters and fracture density.

3. Examples

3.1. Synthetic example

To validate the accuracy of the derived equations, we conducted model testing using data from Well A located in a basin in eastern China. We first obtained the synthetic seismic record by convolving the reflection coefficient from the well with a 30 Hz Ricker wavelet, and Random noise with signal-to-noise ratio of 2 is added. Fig. 4 shows the synthetic seismogram without noise, and Fig. 5 shows the synthetic seismogram with signal-to-noise ratio of 2.

Fig. 6 presents the inversion results for both four-parameter and six-parameter models, with the former based on Eq. (7) and the latter on Eq. (5), under noise-free conditions. Fig. 7 shows the relative errors corresponding to these inversion outcomes. The analysis indicates that the inversion accuracy for the background elastic parameters is relatively high, while the accuracy for fracture

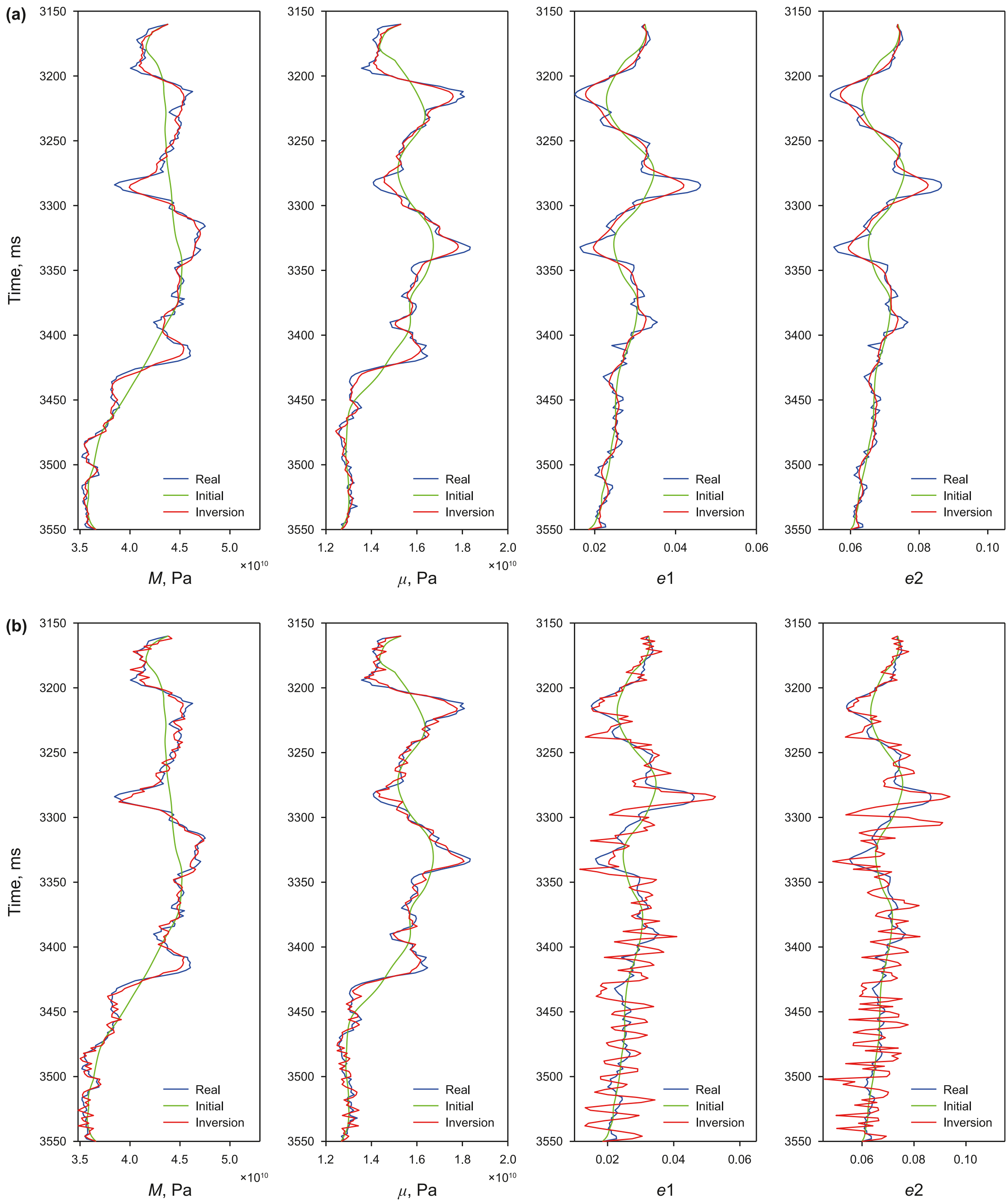

Fig. 8. The inversion results with $S/N = 2$. **(a)** Four parameter inversion results; **(b)** six parameter indirect inversion results.

density remains lower. This discrepancy is primarily attributed to the inherent limitations of the inversion method itself, such as wavelet errors and the lack of a robust inversion algorithm.

Further evaluation of the inversion results in the presence of noise, specifically for a signal-to-noise ratio of 2, is illustrated in Fig. 8, with the associated relative errors shown in Fig. 9. Despite the presence of noise, the inversion of background elastic parameters retains a high degree of robustness, with minimal deviation from the noise-free case. In contrast, the inversion accuracy of fracture density is significantly reduced. This degradation can be largely explained by the relatively small value of fracture density, which results in its low sensitivity to the reflection coefficient, thus diminishing the inversion accuracy.

Moreover, the six-parameter inversion demonstrates a marked increase in the error associated with fracture density estimation, with errors approximately twice as large as those observed in the four-parameter inversion. This phenomenon is linked to the inherent instability of the six-parameter inversion method, particularly in the inversion of fracture density, which can lead to divergent results. Additionally, when fracture weakness parameters

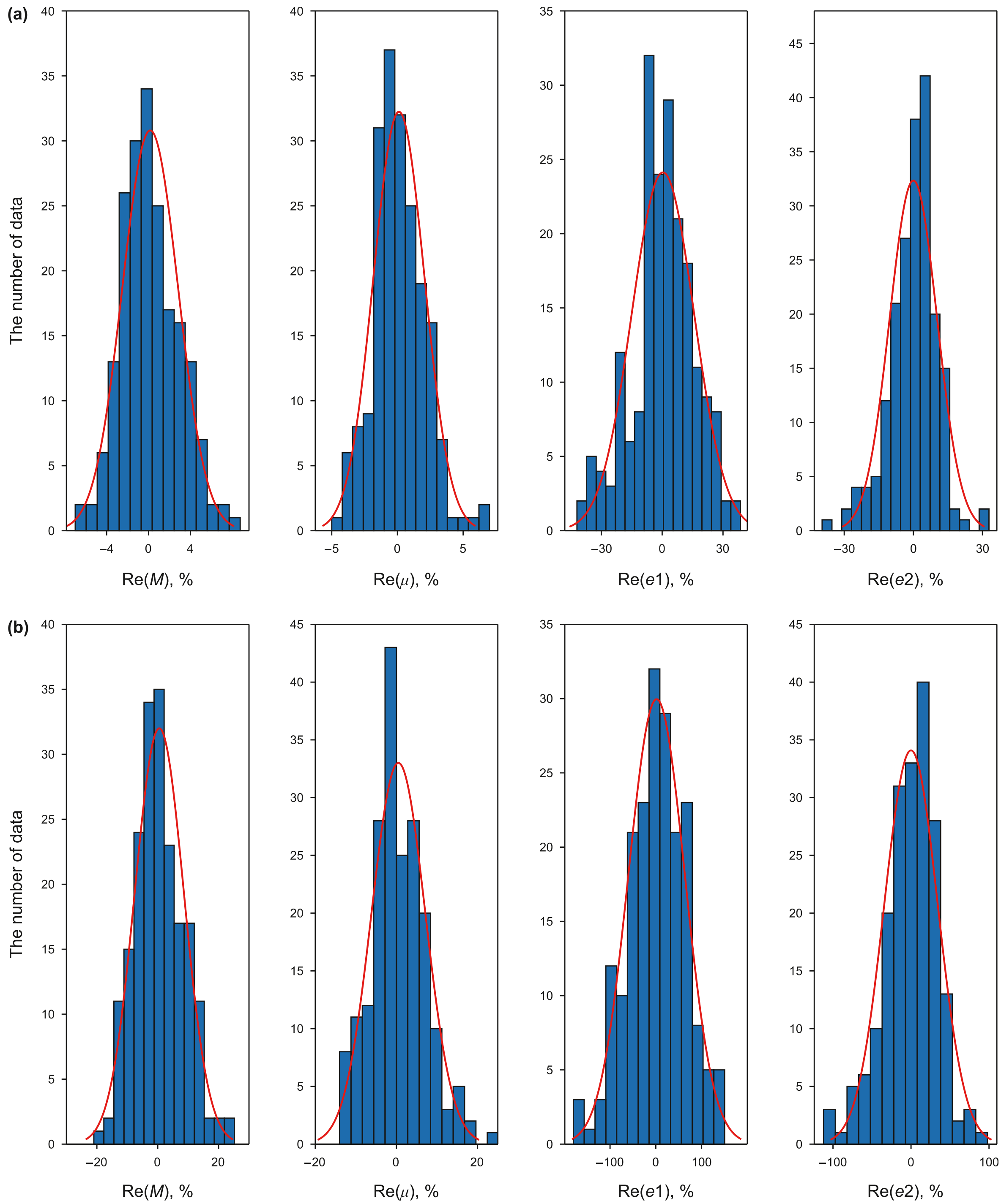

Fig. 9. The inversion error with $S/N = 2$. **(a)** Four parameter inversion error; **(b)** six parameter indirect inversion error.

obtained from the inversion process are used to calculate fracture density, the accumulation of errors further exacerbates the final inversion results for fracture density.

3.2. Field data example

Tight carbonate rocks are mainly developed in the reservoirs of the target work area, and the matrix porosity is generally less than 2%. Effective reservoirs cannot be formed simply by relying on porous reservoirs. Under the influence of the Paleo-Asian Ocean, Tethys Ocean and Pacific Tectonic System, the multi-stage tectonic movement in the Meso-Cenozoic Era triggered the frequent occurrence of fault activities, in which the main basement fault controlled the distribution of fractures in the study area, resulting in the development of two groups of inclined fractures and many micro fractures in the carbonate rocks in the work area. The existence of these fractures significantly improves the permeability of the reservoir, expands the reservoir space, and greatly improves the carbonate reservoir performance, making it a high-quality reservoir.

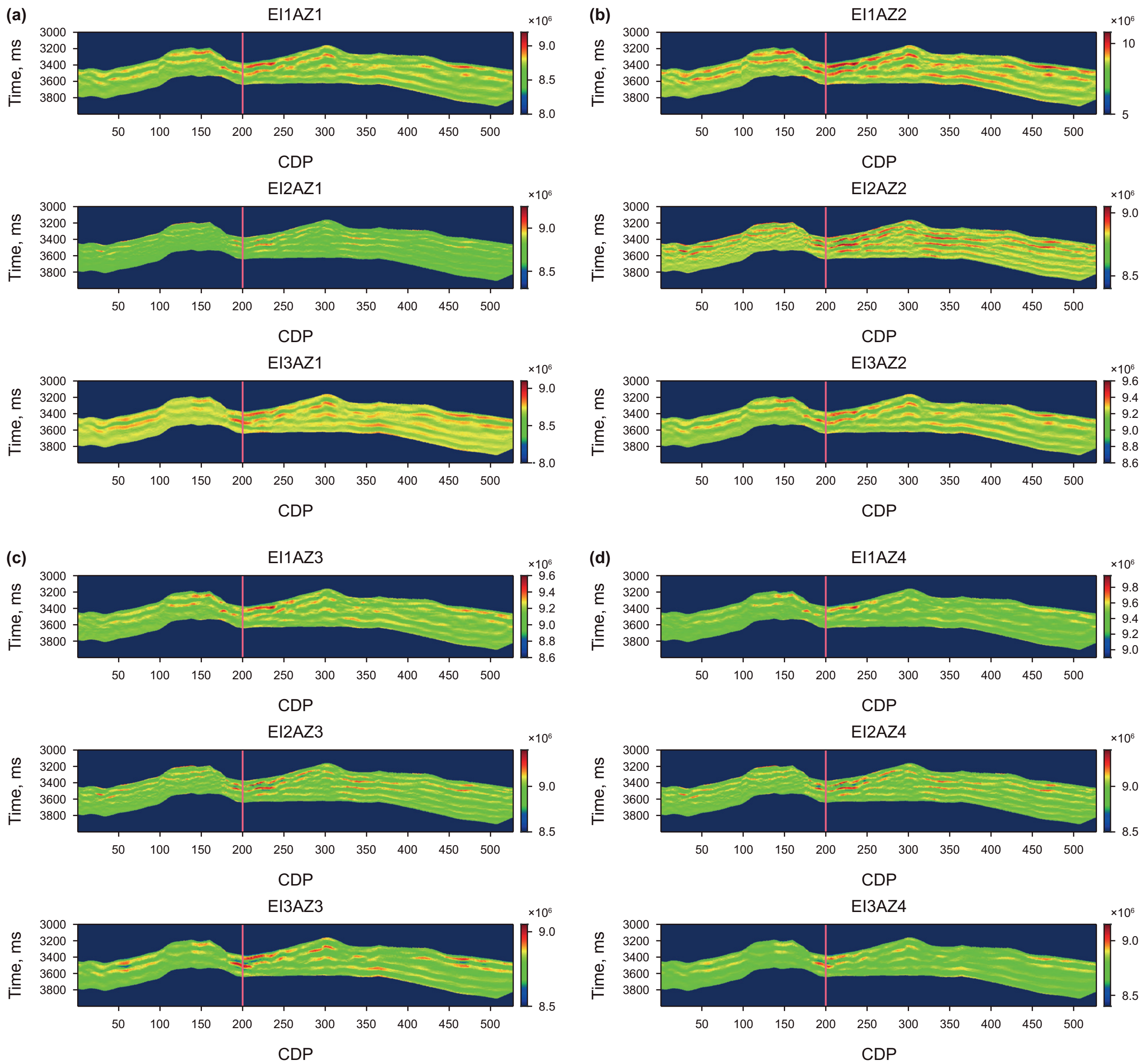

Fig. 10. Azimuth elastic impedance.

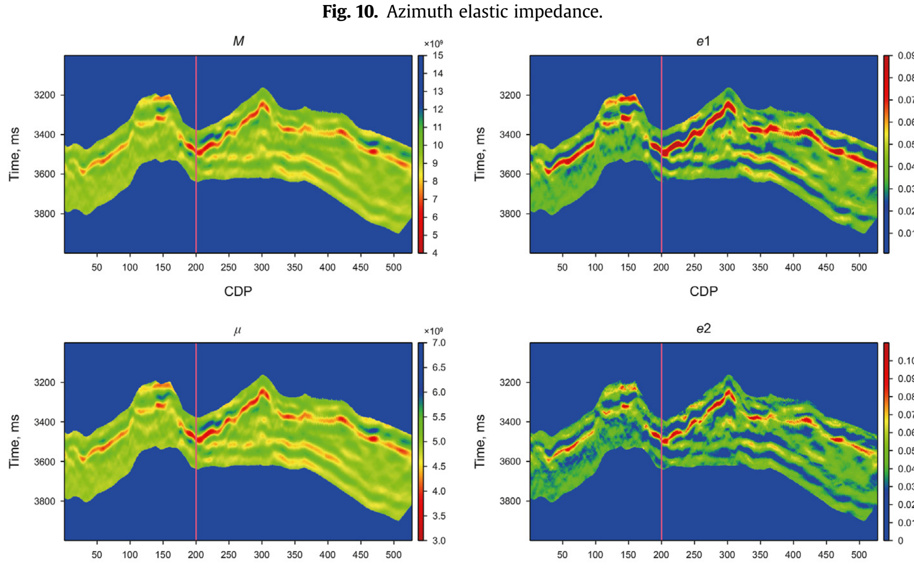

Fig. 11. Inversion parameters.

Preprocessing of seismic data is essential due to the medium's inherent complexity and the instability of the inversion process. Firstly, the offset set is transformed into the angle set, which is then stacked to enhance the signal-to-noise ratio. The angle range for stacking is selected based on the distribution of angles and azimuths in the angle set. The angle distribution of the superimposed seismic data includes incidence angles of 12.5°, 22°, and 30°, and azimuth angles of 30°, 90°, 150°, and 210°. Following these preprocessing steps, we performed elastic impedance inversion using commercial software. Fig. 10 illustrates the results of the elastic impedance inversion obtained through this software.

Fig. 11 presents the longitudinal and transverse wave modulus obtained through azimuth elastic impedance inversion, along with the fracture density for two groups of fractures. We then extracted the bypass channel for comparative analysis. Fig. 12 compares the inversion results with the logging data in the time domain. As can be seen from Fig. 12, for the bypass, the relative errors indicate that the elastic parameter errors fall within −20% to 20%, while the fracture parameter errors range from −50% to 50%. These findings suggest a robust alignment of the inversion results with the well-log data. Furthermore, imaging logging results corroborate that the concentrated area of fracture development above the well aligns well with the fracture density inversion results.

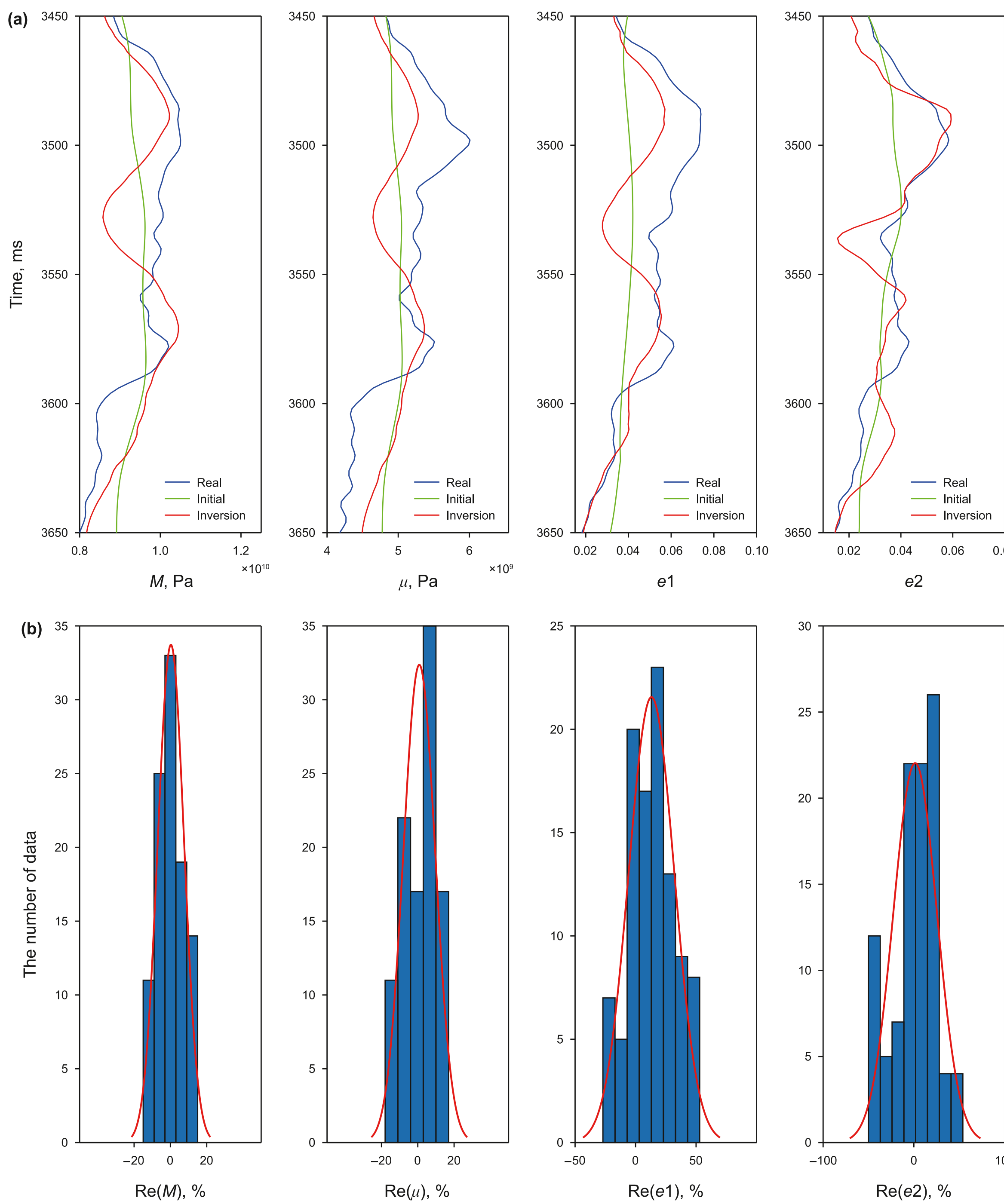

Fig. 12. Inversion results and error at the well location. **(a)** Inversion results, **(b)** inversion error.

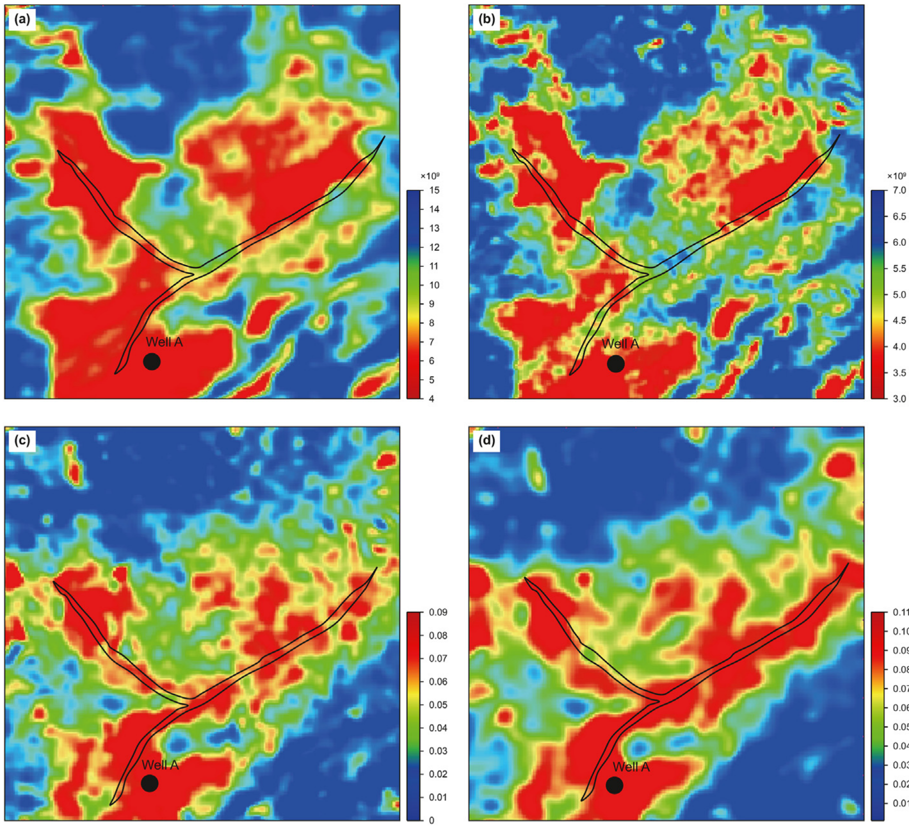

Fig. 13. Inversion parameters time slices. **(a)** M_b, **(b)** μ_b, **(c)** $e1$, **(d)** $e2$.

Table 2
Stability comparison results.

	Model 1	Model 2	Model 3	Model 4
Dip	$\xi_1 = 0^\circ$ $\xi_2 = 0^\circ$	$\xi_1 = 30^\circ$ $\xi_2 = 60^\circ$	$\xi_1 = 45^\circ$ $\xi_2 = 45^\circ$	$\xi_1 = 90^\circ$ $\xi_2 = 90^\circ$
Condition number (four)	264.3	412.1	364.2	512.7
Condition number (six)	2040.3	5608.5	4248.6	6635.2

Fig. 13 illustrates the three-dimensional time slice derived from the inversion results. Notably, the fracture density at the well location exhibits a significantly elevated value, suggesting that the degree of fracture development at this depth is markedly higher in this area. In addition, we project the fault data interpreted by geologists onto time slices to reveal the crack development characteristics in the surrounding area of the fault. The results indicate that the fracture density is higher in areas close to the fault development zone, while areas far away from the fault exhibit lower levels of fracture development. By analyzing the time slice results, we further verified the reliability of the inversion results and proved that this method can effectively predict the favorable distribution areas of reservoirs. Therefore, the inversion results effectively delineate fracture development zones and offer reliable insights for identifying high-quality oil and gas reservoirs.

4. Discussions

In the derivation of the stiffness matrix, the crack weakness parameter and crack inclination have an important impact on the overall stiffness of the medium. The normal weakness of the crack reflects the difference of elastic parameters on both sides of the normal direction of the crack, while the tangential weakness of the crack refers to the difference of elastic parameters on both sides along the tangential direction of the crack. With the increase of crack weakness parameter, the overall stiffness of the medium will decrease significantly, which is more prone to deformation under external force. In addition, the influence of crack dip angle on medium stiffness is mainly reflected in directionality. When the crack dip angle increases to 90°, the deformation ability of the medium increases when the horizontal pressure is applied; When the fracture dip angle decreases to 0°, the medium also shows a strong deformation trend when the vertical pressure is applied.

In the analysis of the contribution of reflection coefficient, the order of magnitude difference between crack parameters and background elastic parameters is a factor that cannot be ignored. Previous studies usually did not fully consider the order of magnitude difference between these parameters when giving model parameters, which may lead to some errors in the estimation of the contribution of reflection coefficient. In order to solve this problem, this paper obtains the reasonable distribution range of the model parameters by analyzing the logging data, and assigns the model parameters based on the 95% confidence interval of the normal distribution. This method can more accurately reflect the actual contribution of each parameter to the reflection coefficient, so as to provide more reliable analysis results of the reflection coefficient contribution. Based on these analysis results, we can effectively select the angle domain seismic data suitable for the inversion target, and improve the accuracy and reliability of the inversion process.

In this study, we compared four-parameter inversion with six-parameter inversion to evaluate the stability of the two methods. For this reason, we assume that the velocity ratio of transverse and longitudinal waves is 1/4, and design four models with different dip angles. Based on these models, the condition numbers of the two inversion methods are calculated. By comparing the results of the condition number (see Table 2), it is obvious that no matter which model is used, the condition number of four-parameter inversion is always lower than that of six-parameter inversion. This shows that the four-parameter inversion method performs better in stability. The smaller condition number means that the four-parameter inversion has better numerical stability in the calculation process, and can more effectively avoid the error amplification. Therefore, the four-parameter inversion method may be more reliable in practical applications, especially in the face of complex geological conditions.

5. Conclusions

To characterize the monoclinic media resulting from two sets of inclined fractures within an isotropic medium, we derive a new reflection coefficient equation and simplify the equation to obtain a reflection coefficient equation with two elastic parameters and two sets of fracture densities with a total of four parameters to be inverted. The accuracy of these equations was verified by synthetic seismic recording tests using well data from a basin in eastern China, as the inversion results closely matched the well data. Further, applying azimuth elastic impedance inversion to actual seismic data successfully delineated the fracture development areas, offering a robust tool for identifying high-quality oil and gas reservoirs.

CRediT authorship contribution statement

Sheng-Zhao Dai: Writing – original draft, Methodology, Investigation, Formal analysis. **Guang-Zhi Zhang:** Writing – review & editing, Software, Investigation, Funding acquisition. **Hong-Jian Hao:** Methodology. **Zhen-Yu Zhu:** Funding acquisition, Data curation. **Zhen-Feng Liu:** Funding acquisition, Data curation. **Zhen Yang:** Formal analysis, Data curation.

Declaration of competing interest

The authors declare that they have no known competing financial interests or personal relationships that could have appeared to influence the work reported in this paper.

Acknowledgment

We would like to express our gratitude for the sponsorship of the National Natural Science Foundation of China under the Special Fund for Basic Research Operations of the Central Universities (U23B6010) and the CNOOC “14th Five Year Plan” Major Science and Technology Project (KJGG2022-0304). Thanks to Geosoftware for Jason software support.

Appendix 1. The comparison of the reflection coefficient equations

When the inclination angle of the two groups of fractures is the same, the two groups of fractures merge into one group of fractures, and the monoclinic medium degenerates into TTI medium, Eq. (5) degenerates as follows:

$$R_{\mathrm{pp}}(\theta,\varphi)=a(\theta)\frac{\Delta M_{\mathrm{b}}}{M_{\mathrm{b}}}+b(\theta)\frac{\Delta\mu_{\mathrm{b}}}{\mu_{\mathrm{b}}}+d(\theta,\varphi)\Delta\delta_{\mathrm{N1}}^{\mathrm{tilted}}+e(\theta,\varphi)\Delta\delta_{\mathrm{T1}}^{\mathrm{tilted}} \tag{11}$$

where $a(\theta), b(\theta), d(\theta,\varphi), e(\theta,\varphi)$ is consistent with that of Eq. (5). The specific form of the TTI medium formula derived by Pan et al. (2021) is as follows:

$$R_{\mathrm{pp}}(\theta,\varphi)=a(\theta)\frac{\Delta M_{\mathrm{b}}}{M_{\mathrm{b}}}+b(\theta)\frac{\Delta\mu_{\mathrm{b}}}{\mu_{\mathrm{b}}}+c(\theta)\frac{\Delta\rho}{\rho}+d_{\delta_{\mathrm{N}}}(\theta,\varphi)\Delta\delta_{\mathrm{N1}}^{\mathrm{tilted}}+e_{\delta_{\mathrm{T}}}(\theta,\varphi)\Delta\delta_{\mathrm{T1}}^{\mathrm{tilted}} \tag{12}$$

where, $a(\theta), b(\theta)$ is consistent with that of Eq. (5), and

$$c(\theta)=\frac{1}{2}-\frac{\sec^2\theta}{4}$$

$$d_{\delta_{\mathrm{N}}}(\theta,\varphi)=-\frac{\sec^2\theta}{4}\begin{bmatrix}\left(\chi_{\mathrm{b}}\cos^2\xi_1+\sin^2\xi_1\right)\sin^4\theta\cos^4\varphi+\left(\cos^2\xi_1+\chi_{\mathrm{b}}\sin^2\xi_1\right)\cos^4\theta\\+2\chi_{\mathrm{b}}\left(\chi_{\mathrm{b}}\cos^2\xi_1+\sin^2\xi_1\right)\sin^4\theta\sin^2\varphi\cos^2\varphi\\+2\chi_{\mathrm{b}}\left(\cos^2\xi_1+\chi_{\mathrm{b}}\sin^2\xi_1\right)\sin^2\theta\cos^2\theta\cos^2\varphi\\\chi_{\mathrm{b}}^2\sin^4\theta\sin^4\varphi-\left(\dfrac{\sin^2 2\xi_1}{2}\left(\chi_{\mathrm{b}}^2-1\right)-2\chi_{\mathrm{b}}\right)\sin^2\theta\cos^2\theta\cos^2\varphi\end{bmatrix}$$

$$e_{\delta_{\mathrm{T}}}(\theta,\varphi)=g\begin{bmatrix}\cos^2\xi_1\left(\sin^2\theta\cos^2\varphi\right)-\dfrac{1}{4}\sin^2 2\xi_1\begin{pmatrix}\sin^2\theta\tan^2\theta\cos^4\varphi\\+\cos^2\theta-2\sin^2\theta\cos^2\varphi\end{pmatrix}\\+\cos^2\xi_1\left(\sin^2\theta\sin^2\varphi\right)-\sin^2\xi_1\sin^2\theta\tan^2\theta\sin^2\varphi\cos^2\varphi\end{bmatrix}$$

where $\chi_b = 1 - 2g$ and ξ_1 is the inclination of the fracture. We ignore the role of density, and we make a second-order approximation of the equation, which is simplified to

$$R_{pp}(\theta,\varphi) = \frac{\sec^2\theta}{4}\frac{\Delta M_b}{M_b} - 2g\sin^2\theta\frac{\Delta\mu_b}{\mu_b} + \begin{bmatrix} -\frac{1}{4}\left(1-2g\sin^2\xi_1\right)^2 + \\ \left(g - 2g\sin^2\xi_1 + g^2\sin^4\xi_1 - \frac{1}{4}\right)\sin^2\theta + \\ \left(\frac{1}{2}g^2\sin^2 2\xi_1 + g^2\sin^2\xi_1\right)\sin^2\theta\cos^2\varphi \end{bmatrix}\Delta\delta_{N1}^{\text{tilted}} + \begin{bmatrix} \left(-\frac{1}{4}g\sin^2 2\xi_1 + \left(g\cos^2\xi_1 + \frac{1}{4}g\sin^2 2\xi_1\right)\sin^2\theta\right. \\ \left.+\left(g\cos^2 2\xi_1 + \frac{1}{2}g\sin^2 2\xi_1 - g\cos^2\xi_1\right)\sin^2\theta\cos^2\varphi\right. \end{bmatrix}\Delta\delta_{T1}^{\text{tilted}} \tag{13}$$

It can be seen that Eq. (13) is the same as Eq. (11).

When the inclination angle of both groups of fractures is 0°, the monoclinic medium degenerates into VTI medium, and Eq. (5) degenerates to

$$R_{pp}(\theta,\varphi) = \frac{\sec^2\theta}{4}\frac{\Delta M_b}{M_b} - 2g\sin^2\theta\frac{\Delta\mu_b}{\mu_b} + \left[\left(-\frac{1}{4} + \left(g - \frac{1}{4}\right)\sin^2\theta\right]\Delta\delta_{N1}^{\text{tilted}} + g\sin^2\theta\Delta\delta_{T1}^{\text{tilted}}\right. \tag{14}$$

This result aligns with the equation established by Pan et al. (2021).

In the case where both fracture groups are inclined at 90°, the monoclinic medium simplifies into an HTI medium, leading to a reduction of Eq. (5) to

$$R_{pp}(\theta,\varphi) = \frac{\sec^2\theta}{4}\frac{\Delta M_b}{M_b} - 2g\sin^2\theta\frac{\Delta\mu_b}{\mu_b} + \begin{bmatrix} \left(-\frac{1}{4}(1-2g)^2 + \left(g^2 - g - \frac{1}{4}\right)\sin^2\theta\right. \\ +g^2\sin^2\theta\cos^2\varphi \end{bmatrix}\Delta\delta_{N1}^{\text{tilted}} + g\sin^2\theta\cos^2\varphi\Delta\delta_{T1}^{\text{tilted}} \tag{15}$$

This result aligns with the equation established by Chen et al. (2017).

When one group of fractures has an inclination angle of 90° and another group of fractures has an inclination angle of 0°, the medium degenerates into OA medium, and Eq. (5) degenerates as:

$$R_{pp}(\theta,\varphi) = \frac{\sec^2\theta}{4}\frac{\Delta M_b}{M_b} - 2g\sin^2\theta\frac{\Delta\mu_b}{\mu_b} + \left[\left(-\frac{1}{4} + \left(g - \frac{1}{4}\right)\sin^2\theta\right]\Delta\delta_{N1}^{\text{tilted}} + g\sin^2\theta\Delta\delta_{T1}^{\text{tilted}}\right. + \begin{bmatrix} \left(-\frac{1}{4}(1-2g)^2 + \left(g^2 - g - \frac{1}{4}\right)\sin^2\theta\right. \\ +g^2\sin^2\theta\cos^2\varphi \end{bmatrix}\Delta\delta_{N2}^{\text{tilted}} + g\sin^2\theta\cos^2\varphi\Delta\delta_{T2}^{\text{tilted}} \tag{16}$$

This result aligns with the equation established by Zhang et al. (2020).

References

Bakulin, A., Grechka, V., Tsvankin, I., 2000a. Estimation of fracture parameters from reflection seismic data—Part I: HTI model due to a single fracture set. Geophysics 65 (6), 1788–1802. https://doi.org/10.1190/1.1444863.

Bakulin, A., Grechka, V., Tsvankin, I., 2000b. Estimation of fracture parameters from reflection seismic data—Part III: fractured models with monoclinic symmetry. Geophysics 65 (6), 1818–1830. https://doi.org/10.1190/1.1444865.

Cambois, G., 2000. AVO inversion and elastic impedance. SEG Expanded Abstract 2000, pp. 142–145. https://doi.org/10.1190/1.1815671.

Chen, H., Pan, X., Ji, Y., et al., 2017. Bayesian Markov chain Monte Carlo inversion for weak anisotropy parameters and fracture weaknesses using azimuthal elastic impedance. Geophys. J. Int. 210 (2), 801–818. https://doi.org/10.1093/gji/ggx196.

Chen, H., Zhang, G., Chen, J., et al., 2014. Fracture filling fluids identification using azimuthally elastic impedance based on rock physics. J. Appl. Geophys. 110, 98–105. https://doi.org/10.1016/j.jappgeo.2014.09.006.

Guo, Z., Zhang, X., Liu, C., 2022a. An improved scheme of azimuthally anisotropic seismic inversion for fracture prediction in volcanic gas reservoirs. IEEE Trans. Geosci. Rem. Sens. 60, 1–12. https://doi.org/10.1109/TGRS.2022.3186426.

Guo, Z., Zhang, X., Liu, C., et al., 2022b. Hydrocarbon identification and bedding fracture detection in shale gas reservoirs based on a novel seismic dispersion attribute inversion method. Surv. Geophys. 43 (6), 1793–1816. https://doi.org/10.1007/s10712-022-09726-z.

Jílek, P., 2002. Converted PS-wave reflection coefficients in weakly anisotropic media. Pure Appl. Geophys. 159, 1527–1562. https://doi.org/10.1007/s00024-002-8696-9.

Li, Y., Guo, Z., Liu, C., 2024. Characterization of fluid-saturated fractures based on seismic azimuthal anisotropy dispersion inversion method. IEEE Trans. Geosci. Rem. Sens. 62, 1–17. https://doi.org/10.1109/TGRS.2024.3407134.

Martins, J.L., 2006. Elastic impedance in weakly anisotropic media. Geophysics 71 (3), D73–D83. https://doi.org/10.1190/1.2195448.

Pan, X., Li, L., Zhou, S., et al., 2021. Azimuthal amplitude variation with offset parameterization and inversion for fracture weaknesses in tilted transversely isotropic media. Geophysics 86 (1), C1–C18. https://doi.org/10.1190/geo2019-0215.1.

Pan, X., Zhang, G., Yin, X., 2019. Azimuthally anisotropic elastic impedance parameterisation and inversion for anisotropy in weakly orthorhombic media. Explor. Geophys. 50 (4), 376–395. https://doi.org/10.1080/08123985.2019.1606199.

Pan, X., Lu, C., Zhang, G., et al., 2022. Seismic characterization of naturally fractured reservoirs with monoclinic symmetry induced by horizontal and tilted fractures from amplitude variation with offset and azimuth. Surv. Geophys. 43 (3), 815–851. https://doi.org/10.1007/s10712-022-09709-0.

Pan, X., Zhao, Z., 2024. A decoupled fracture-and stress-induced PP-wave reflection coefficient approximation for azimuthal seismic inversion in stressed horizontal transversely isotropic media. Surv. Geophys. 45 (1), 151–182. https://doi.org/10.1007/s10712-023-09791-y.

Rüger, A., 1997. P-wave reflection coefficients for transversely isotropic models with vertical and horizontal axis of symmetry. Geophysics 62, 713–722. https://doi.org/10.1190/1.1444181.

Rüger, A., 1998. Variation of P-wave reflectivity with offset and azimuth in anisotropic media. Geophysics 63, 935–947. https://doi.org/10.1190/1.1444405.

Schoenberg, M., 1980. Elastic wave behavior across linear slip interfaces. J. Acoust. Soc. Am. 68 (5), 1516–1521. https://doi.org/10.1121/1.385077.

Schoenberg, M., Sayers, C.M., 1995. Seismic anisotropy of fractured rock. Geophysics 60 (1), 204–211. https://doi.org/10.1190/1.1443748.

Shaw, R.K., Sen, M.K., 2004. Born integral, stationary phase and linearized reflection coefficients in weak anisotropic media. Geophys. J. Int. 158 (1), 225–238. https://doi.org/10.1111/j.1365-246X.2004.02283.x.

Zhang, G., Li, L., Pan, X., et al., 2020. Azimuthal Fourier coefficient inversion for horizontal and vertical fracture characterization in weakly orthorhombic media. Geophysics 85 (6), C199–C214. https://doi.org/10.1190/geo2019-0797.1.

Zhao, Y., Wen, X.T., Li, C.L., et al., 2024. Systematic prediction of the gas content, fractures, and brittleness in fractured shale reservoirs with TTI medium. Pet. Sci. 21 (5), 3202–3221. https://doi.org/10.1016/j.petsci.2024.04.015.

Zong, Z., Yin, X., Wu, G., 2013. Elastic impedance parameterization and inversion with Young's modulus and Poisson's ratio. Geophysics 78 (6), N35–N42. https://doi.org/10.1190/geo2012-0529.1.